1 **The role of advection and dispersion in the rock matrix on the transport of leaking CO_2-**

2 **saturated brine along a fractured zone**

3 Nawaz Ahmad[a, b,*], Anders Wörman[a], Xavier Sanchez-Vila[c], and Andrea Bottacin-

4 Busolin[d]

5 [a] Department of Civil and Architectural Engineering, KTH Royal Institute of Technology,

6 Brinellvägen 23, 10044, Stockholm, Sweden

7 [b] Policy Wing, Ministry of Petroleum and Natural Resources, Government of Pakistan,

8 Pakistan

9 [c] Hydrogeology Group, Department of Geotechnical Engineering and Geosciences,

10 Universitat Politècnica de Catalunya, UPC-BarcelonaTech, 08034 Barcelona, Spain

11 [d] School of Mechanical, Aerospace and Civil Engineering, University of Manchester, United

12 Kingdom

13 *Correspondence author at: Department of Civil and Architectural Engineering, KTH Royal

14 Institute of Technology, Brinellvägen 23, 10044, Stockholm, Sweden.

15 E-mail address: nawaza@kth.se

16 **Running Title:** Reactive transport of CO_2-saturated brine along a fractured zone

17 **1**

18

19

---

[1] COMSOL code is available upon request from the author.

Abstract: CO_2 that is injected into a storage reservoir can leak in dissolved form because of brine displacement from the reservoir, which is caused by large-scale groundwater motion. Simulations of the reactive transport of leaking CO_{2aq} along a conducting fracture in a clay-rich caprock are conducted to analyze the effect of various physical and geochemical processes. Whilst several modelling transport studies along rock fractures have considered diffusion as the only transport process in the surrounding rock matrix (diffusive transport), this study analyzes the combined role of advection and dispersion in the rock matrix in addition to diffusion (advection-dominated transport) on the migration of CO_{2aq} along a leakage pathway and its conversion in geochemical reactions. A sensitivity analysis is performed to quantify the effect of fluid velocity and dispersivity. Variations in the porosity and permeability of the medium are observed in response to calcite dissolution and precipitation along the leakage pathway. We observe that advection and dispersion in the rock matrix play a significant role in the overall transport process. For the parameters that were used in this study, advection-dominated transport increased the leakage of CO_{2aq} from the reservoir by nearly 305%, caused faster transport and increased the mass conversion of CO_{2aq} in geochemical reactions along the transport pathway by approximately 12.20% compared to diffusive transport.

1. Introduction

CO$_2$ storage in geological formations is a method to slow the atmospheric accumulation of greenhouse gases (Holloway, 2005; Middleton et al., 2012). Environmental hazards that are related to geological CO$_2$ storage are associated with its potential leakage from storage reservoirs (Stone et al., 2009; Haugan and Joos, 2004). The leakage risk is the greatest when the injected CO$_2$ remains as a supercritical free-phase (CO$_2$) in the reservoir because of its lower density than the resident fluid (Pruess, 2006a, 2006b). However, the leakage risk diminishes with time because of the progressive dissolution of supercritical CO$_2$ in the formation fluid (IPCC, 2005). Upon the complete dissolution of CO$_2$ in the formation fluid (over 10,000 years), the leakage risk is only associated with the dissolved phase (CO$_{2aq}$) (Bachu et al., 1994).

Recently, a relatively safer method of CO$_2$ geological sequestration has been investigated, in which brine that carries CO$_{2aq}$ is injected into the reservoir rather than supercritical CO$_2$ (Aradóttir et al., 2012; Gislason and Oelkers, 2014). The downward movement of this brine that carries CO$_{2aq}$ is expected because the injected fluid is denser than the resident one. This mode of sequestration exhibits relatively faster and higher consumption of CO$_{2aq}$ through mineral trapping (Aradóttir et al., 2012). However, large-scale groundwater motion may displace the brine from the reservoir, creating an associated risk of CO$_{2aq}$ leakage (Bachu et al., 1994; IPCC, 2005; Gaus, 2010).

The transport of CO$_{2aq}$ may occur through a combination of processes, including advection, dispersion, and diffusion (Bachu et al., 1994). In some cases, fractures or faults may serve as the main leakage pathways (Grisak and Pickens, 2007). Leaking CO$_{2aq}$ may undergo various physical and geochemical interactions with the rock formation. Mass exchange between the conducting fracture and the rock matrix, sorption, and geochemical reactions may immobilize

66 solute species in the fractured rocks (Neretnieks, 1980; Cvetkovic et al., 1999; Xu et al., 2001;

67 Bodin et al., 2003). Low-pH brine that carries CO_{2aq} may potentially undergo various

68 geochemical reactions with its associated conversion through calcite dissolution or

69 precipitation reactions (Dreybrodt et al., 1996; Kaufmann and Dreybrodt, 2007; Dreybrodt et

70 al., 1997). Variations in the medium's porosity and permeability may result from mineral

71 dissolution or precipitation because of geochemical interactions with leaking CO_2-saturated

72 brine. For example, the fast dissolution of carbonate minerals may widen the existing flow

73 paths (Andreani et al., 2008; Gaus, 2010; Ellis et al., 2011(a, b)).

74 Gherardi et al. (2007) analyzed the geochemical interactions of leaking CO_2 and associated

75 brine that carries CO_{2aq} by means of numerical studies and reported porosity variations near

76 the reservoir-caprock interface, which are mainly related to calcite mineral reactions. In an

77 experimental study, Andreani et al. (2008) reported a 50% increase in the medium's porosity

78 in close proximity of the fracture because of calcite dissolution from cyclic flows of CO_2 and

79 CO_2-saturated brine. Noiriel et al. (2007) examined the effects of acidic water in a flow-

80 through experiment and reported the faster dissolution of carbonate minerals compared to clay

81 minerals in the fracture. Ellis et al. (2011a) performed a seven-day experiment to study the

82 geochemical evolution of flow pathway in fractured carbonate caprock because of leaking

83 CO_{2aq}-carrying brine. These authors reported an increase in fracture apertures because of the

84 preferential dissolution of calcite mineral. Ellis et al. (2011b) reported a flow-through

85 experiment of acidic brine in fractured carbonate caprock (over 90% of the bulk rock

86 composed of calcite and dolomite), which increased the fracture apertures close to the inlet

87 boundary because of preferential calcite dissolution.

88 Peters et al. (2014) suggested including the complex geochemical interactions of CO_2-

89 saturated brine with mineral calcite in reactive transport models to investigate the

90 permeability evolution of flow pathways in caprock. Nogues et al. (2013) suggested

91 disregarding minerals such as kaolinite, anorthite, and albite in geochemical models that

92 involve the fate of CO_2-saturated water whenever carbonate minerals are abundant. Several

93 authors conceptualized solute transport in a fracture-matrix system as a dual-domain model;

94 transport in fractures occurs through advection, dispersion and diffusion, whereas diffusion

95 alone is considered in the matrix (Steefel and Lichtner, 1998a, 1998b; Novak, 1993, 1996;

96 Ahmad et al., 2015).

97 In this study, we consider the presence of an altered rock matrix zone (where advection and

98 dispersion may not be negligible) that surrounds a fracture and how these processes affect the

99 reactive transport of CO_2-saturated brine that is leaking along this fracture-matrix system. The

100 velocity fields in the fracture and rock matrix are modelled by Brinkman equations while

101 considering the time- and space-dependent variations in porosity and permeability that are

102 caused by the dissolution and precipitation of calcite. Various transport scenarios are

103 simulated for a period of 500 years to analyze the significance of adding advection and

104 dispersion into the rock matrix compared to diffusion alone (diffusive transport) on the fate of

105 leaking CO_{2aq} and its conversion in geochemical reactions along the leakage pathway. A

106 comparative analysis between various reactive transport scenarios is presented in terms of

107 variations in the medium's porosity, CO_{2aq} leakage fluxes from the reservoir, the retention of

108 CO_{2aq} because of mass that is stored in aqueous and adsorbed states, and CO_{2aq} that is

109 converted in geochemical reactions along the leakage pathway. A sensitivity analysis is also

110 performed to determine the significance of the fluid velocity and dispersivity.

111 **2. Model description**

112 The formulation of the reactive transport problem involves a series of mass balance

113 and momentum equations combined with constitutive thermodynamic relationships.

114 The reactions that are considered in the study are displayed in Table 1. Reactions (R0)-

(R4) were considered to be fast and modelled as in equilibrium, whereas the calcite

mineral reaction (R5) was considered a slow (kinetically controlled), reversible

reaction. Reaction (R0) represents the equilibrium between supercritical CO_2 and

CO_{2aq} and was only included in the batch geochemical models but excluded in the

subsequent reactive transport modelling. The solubility of CO_2 in the fluid (reaction

(R0)) was based on the relationships that were developed by Duan and Sun (2003) and

later modified by Duan et al. (2006). This solubility model is valid for a wide range of

pressures, temperatures, and ionic strengths. The equilibrium constants for remaining

reactions (R1)-(R5) were obtained from the LLNL thermo database (Delany and

Lundeen, 1990), the default thermodynamic database for The Geochemist's

Workbench$^{®}$ (GWB), an integrated geochemical modelling package. Linear

interpolation was used to compute the equilibrium constants of the reactions at the

temperature that was used in the study. The activity coefficient of CO_{2aq} was computed

from the model that was presented by Duan and Sun (2003). The B-dot model, an

extension of the Debye-Hückel equation, was used to compute the activity coefficients

of the involved aqueous species (Bethke, 2008).

Table 1. Chemical reactions that were considered for the $CaCO_3$-H_2O-CO_2 system.

No.	Reaction
(R0)	$CO_{2g} \leftrightarrow CO_{2aq}$
(R1)	$H_2O + CO_{2aq} \leftrightarrow H^+ + HCO_3^-$
(R2)	$H_2O \leftrightarrow H^+ + OH^-$
(R3)	$HCO_3^- \leftrightarrow H^+ + CO_3^{2-}$
(R4)	$Na^+ + HCO_3^- \leftrightarrow NaHCO_{3aq}$
(R5)	$CaCO_3 + H^+ \leftrightarrow Ca^{2+} + HCO_3^-$

2.1. Model domain

Fig. 1 presents the schematic of a CO_2 storage reservoir that is overlain by a clay-rich caprock with a vertical conducting fracture. The domain involves a conducting fracture that is surrounded by a less-permeable rock matrix. W_f is the half-width of the fracture (taken as 1 mm), W_m is the half-width of the rock matrix (50 m), and L is the caprock length (100 m). The fracture is assumed to be partially filled with porous material (Wealthall et al., 2001; Wu et al., 2010; Laubach et al., 2010; Liu et al., 2013) and has an initial porosity of 0.60. The porosity of the rock matrix is taken as 0.12. The lower boundary of the caprock, and thus the upper boundary of the reservoir, is assumed to be at a depth of 1040 m below the land surface. The leaking CO_2-saturated brine from the reservoir enters the transport domain from the bottom inflow boundary, which comprises a fracture and rock matrix, and exits through the top (open) boundary. Continuity conditions for the solute and fluid mass are applied at the fracture-matrix interface. Symmetry with no-flow conditions are assumed at the left (center of the fracture) and right (center of rock matrix) boundaries.
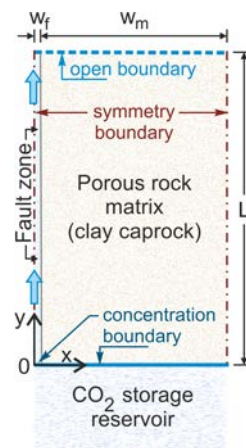
Figure 1. Schematic of the transport domain (clay-rich caprock with a vertical conducting fracture) that overlies the CO_2 storage reservoir.

2.2. Reactive transport of aqueous species

153 The transport of aqueous species is defined by the following system of equations, which are

154 written in terms of the chemical component species (COMSOL; Ahmad et al., 2015):

$$\mathbf{R_f}\theta \frac{\partial \mathbf{u}}{\partial t} + \left(1 - \mathbf{K_d}\rho_p\right)\mathbf{u}\frac{\partial \theta}{\partial t} - \nabla \cdot [(\mathbf{D_D} + \mathbf{D_e})\nabla \mathbf{u}] + \nabla \cdot (\mathbf{vu}) = \theta \mathbf{r_{kin}} \quad (1)$$

155

$$\mathbf{R_f} = 1 + \frac{\rho_{bulk}}{\theta}\mathbf{K_d} \quad (1b)$$

156

157 where $\mathbf{u}$ (x,y,t) is the vector of the concentration [mol/(kg water)] of the component

158 species; $\mathbf{R_f}$ (x,y,t) is a diagonal matrix of the retardation factor, which considers

159 sorption on the surface of the immobile mineral phases; $\mathbf{K_d}$ (x,y,t) is a diagonal matrix

160 where the elements include the sorption partition coefficients of the component species

161 [m^3/kg]; $\rho_{bulk} = (1 - \theta)\rho_p$ is the bulk density [kg/m^3] of the porous media; θ(x,y,t) is

162 the spatially and temporally varying porosity of the medium; ρ_p(x,y,t) is the particle

163 density [kg/m^3]; $\mathbf{D_D}$ is the dispersion tensor [m^2/s]; $\mathbf{D_e} = \theta D_b \mathbf{I}$ is the effective

164 diffusion diagonal tensor [m^2/s] with $\mathbf{I}$ as the identity tensor; D_b is the diffusion

165 coefficient of CO_{2aq} in brine; $\mathbf{v}$ (x,y,t) is the specific flux [m/s], which is updated in

166 space and time; and $\mathbf{r_{kin}}$ (x,y,t) [mol/(s-kg water)] is the reaction term, which considers

167 the consumption or production of component species from geochemical reactions

168 ((R1)-(R5) in Table 1). The diffusion coefficient of CO_{2aq} in brine is computed at the

169 pressure and temperature conditions that are used in this study from the relationships

170 by Al-Rawajfeh (2004) and Hassanzadeh et al. (2008). The computed diffusion

171 coefficient of CO_{2aq} in brine (3.05×10^{-9} m^2/s) is considered for all the component

172 species (Gherardi et al., 2007). The dispersion tensor in Eq. (1) is defined as a function

173 of the dispersivity and the components of the fluid velocity by the following

174 relationships (Bear, 1972):

$$\begin{cases} D_{Dxx} = \alpha_L \dfrac{v_x^2}{|v|} + \alpha_T \dfrac{v_y^2}{|v|} \\[2mm] D_{Dyy} = \alpha_L \dfrac{v_y^2}{|v|} + \alpha_T \dfrac{v_x^2}{|v|} \\[2mm] D_{Dxy} = D_{Dyx} = (\alpha_L - \alpha_T) \dfrac{v_x v_y}{|v|} \end{cases} \qquad (2)$$

175   where α_L and α_T are the longitudinal and transverse dispersivity, respectively.

176   The transport Eq. (1) is written in terms of the component species (**u**), which are linear

177   combinations of aqueous species that are unaffected by equilibrium reactions. The

178   methodology of Saaltink et al. (1998) allows us to express the mass conservation of

179   aqueous species and write the source/sink terms (**r**$_{kin}$) in terms of the chemical

180   components. The concentration of aqueous species at every node in the computational

181   domain is then computed by solving the algebraic equations that relate the components

182   and aqueous species (speciation process, see Appendix A). In this study, eight aqueous

183   chemical species in the reaction system ((R1) to (R5) in Table 1) are transformed into

184   four component species. Therefore, **u** is a vector of size 4 and $\mathbf{R_f}$ and $\mathbf{K_d}$ are matrices

185   of size 4×4. Eq. (1) is a system of nonlinear partial differential equations in which the

186   variables θ, ρ_p, and ρ_{bulk}, the matrices $\mathbf{R_f}$ and $\mathbf{K_d}$ and the vector $\mathbf{r_{kin}}$ are nonlinear

187   functions of the local concentration of the component species (u).

188   *2.3. Mass conservation of calcite mineral*

189   The mass conservation of calcite mineral that undergoes kinetic reaction in the

190   transport domain (fracture and rock matrix) is modelled by using the following

191   ordinary differential equation (ODE):

192                              $\dfrac{\partial c_{m,bulk}}{\partial t} = -\theta \rho_b r_m$ (3)

193   where $c_{m,bulk}$ (x, y, t) is the concentration of mineral calcite per unit bulk volume

194   [mol/m^3], and the reaction term r_m (x, y, t) represents the consumption (dissolution) or

195   production (precipitation) of calcite [mol/(s-kg water)]. The initial mineral

196   concentration ($c_{m,bulk}$) values are computed to be 3142.03 and 6912.46 mol/m^3 in the

197   fracture and the rock matrix, respectively, based on the corresponding initial volume

198   fraction of calcite (Table 2).

199   **Table** 2. Caprock mineralogical composition in the fracture and the rock matrix.

Mineral	Mineral volume fraction in unaltered rock (Gherardi et al., 2007)	Mineral volume fraction in the fracture for 0.60 porosity	Mineral volume fraction in the rock matrix for 0.12 porosity
Calcite	0.290	0.116	0.255
Dolomite	0.040	0.016	0.035
Quartz	0.200	0.080	0.176
Illite	0.020	0.008	0.018
K-feldspar	0	0	0
Chlorite	0.060	0.024	0.053
Albite	0	0	0
Kaolinite	0.050	0.020	0.044
Na-smectite	0.150	0.060	0.132
Muscovite	0.190	0.076	0.1672

200

201   *2.4. Mineral kinetic reaction*

202   The mineral kinetic reaction (r_m) in Eq. (3) is defined in terms of the species concentration

203   and mineral reactive surface area (Lasaga, 1994):

204    $$r_m = k_m A_m [1 - \Omega_m] \qquad (4)$$

205   where k_m is the temperature-dependent kinetic rate constant of the mineral [mol/(s-m^2)] and

206   A_m is the reactive surface area of the mineral [m^2/(kg water)], which is updated in time and

207   space during the modeling process. The term $\Omega_m = Q_m/K_{eq}$ is the saturation state of calcite,

208   where Q_m represents the calcite ion activity product, and K_{eq} is the equilibrium constant for

209   the mineral reaction. The mineral dissolves in the solution if the saturation state of the brine

210   solution with respect to the mineral is less than unity and precipitates if $\Omega_m > 1$. The

211   temperature dependence of the kinetic rate constant (k_m) of the mineral is described by the

212   Arrhenius equation (Lasaga, 1984):

213
$$k_m = k_{25}\, exp\left[-\frac{E_a}{R}\left(\frac{1}{T} - \frac{1}{298.15}\right)\right] \qquad (5)$$

214   where R (= 8.314 J/(mol-K) is the gas constant; T is the temperature [K]. E_a is the

215   activation energy of calcite, and k_{25} is a reaction constant, which are set to 41.87

216   KJ/mol and 1.60×10^{-9} mol/(s-m^2), respectively, at 25°C (Svensson and Dreybrodt,

217   1992).

218   *2.5. Mineral reactive surface area*

219   The geometric approach is adopted to calculate the mineral reactive surface from the number

220   of mineral grains (Johnson et al., 2004; Marini, 2007). The initial mineral reactive surface

221   area (A_m) values are calculated to be 3.52 and 38.67 m^2/(kg water) in the fracture and rock

222   matrix, respectively, based on the initial volume fractions of calcite in Table 2. The mineral

223   kinetic reaction causes variations in the number of mineral grains and, thus, in the reactive

224   surface area. The following relationship models the variations in the reactive surface area of

225   the mineral:

226
$$A_m = 0.1\left(\frac{A_g}{\theta \rho_b V_g}\right)\left(MV c_{m,bulk}\right) \qquad (6)$$

227   where A_g and V_g are the physical surface area and volume of a mineral grain, respectively

228   (assumed to be spherical with a radius of 1.65×10^{-5} m); MV is the molar volume of the

229   mineral; and $c_{m,bulk}$ is the concentration of the mineral, which varies in time and space

230   because of the mineral kinetic reaction (3). The mineral reactive surface area is set to 10% of

231   its computed physical surface area (Johnson et al., 2004).

232   *2.6. Velocity field for the transport system*

233   The velocity field in the fracture and rock matrix is defined by the Brinkman equations,

234   where flow in porous media is described by a combination of the mass and momentum

235   balances:

$$\frac{\partial(\theta\rho_b)}{\partial t} + \nabla \cdot (\rho_b \mathbf{v}) = 0 \qquad (7)$$

236

$$\frac{\rho_b}{\theta}\left[\frac{\partial \mathbf{v}}{\partial t} + (\mathbf{v} \cdot \nabla)\frac{\mathbf{v}}{\theta}\right] = -\nabla p + \nabla \cdot \left[\frac{\mu_b}{\theta}\left\{(\nabla\mathbf{v} + (\nabla\mathbf{v})^T) - \frac{2}{3}(\nabla \cdot \mathbf{v})\mathbf{I}\right\}\right] - \left(\frac{\mu_b}{\kappa}\right)\mathbf{v} + \mathbf{F} \qquad (8)$$

237

238   where ρ_b is the density [kg/m^3] and μ_b is the dynamic viscosity [kg/(m-s)] of CO_2-

239   saturated brine; p is the pressure [Pa]; and κ is the permeability of the porous medium

240   [m^2]. Gravity is included through the force term ($\boldsymbol{F} = -\rho_b\mathbf{g}$), where $\mathbf{g}$ is the

241   gravitational acceleration vector [9.81 m/s^2]. The brine density and viscosity are equal

242   to 1000 kg/m^3 and 6.27×10^{-4} kg/(m-s), respectively. The viscosity of the brine is

243   computed from the model by Mao and Duan (2009) at 45°C and 105×10^5 Pa

244   (representing conditions at the lower boundary of the domain, which is assumed to be

245   at a depth of 1040 m below the surface). The Brinkman equations expand Darcy's law

246   by including an additional term that considers viscous transport in the momentum

247   equation while treating both the pressure gradient and flow velocity as independent

248   vectors. Popov et al. (2009) found that the Stokes-Brinkman equation can represent

249   porous media that is coupled to free flow regions such as fractures, vugs, and caves,

250   including material fill-in and suspended solid particles. The Brinkman equation is

251   numerically attractive because it defines the flow field in two regions (free flow and

252   porous media) by using only a single system of equations instead of a two-domain

253   approach (Gulbranson et al., 2010). The validity of the Brinkman equations in

254   COMSOL for modelling flow in porous media has been reported in several works

255   (e.g., Sajjadi et al., 2014; Chabonan et al., 2015; Golfier et al., 2015; Basirat et al.,

256   2015).

257   *2.7. Medium's porosity*

258   The variations in the porosity of the porous medium from mineral dissolution and

259   precipitation are modelled in time and space (in fracture and rock matrix) based on the

260   updated volume fraction of the calcite mineral through the following relationship:

261    $$\theta = 1 - VF_{rock,p} \qquad (9)$$

262   where $VF_{rock,p} = \sum_m VF_{m,p}$ is the summation of the volume fractions of all the minerals

263   forming the rock, and $VF_{m,p} = V_{m,p}/V_{rock,p}$ [-] represents the volume fraction (ratio of

264   the mineral volume to the total bulk volume) of each mineral. Some numerical

265   restrictions are applied (Xu et al., 2014): (i) the minimum threshold value of the

266   mineral concentration is set to 1×10^{-7} mol/m^3 to avoid the complete dissolution and

267   corresponding disappearance of the mineral from the domain, and (ii) the minimum

268   porosity of the medium is set to 1×10^{-3} to stop any further mineral precipitation below

269   this value.

270   *2.8. Medium's permeability*

271   The medium's initial permeability is calculated by using the Kozeny-Carman relationship

272   (e.g., Bear and Chang, 2010):

273    $$\kappa_0 = C \frac{\theta_0^3}{(1-\theta_0)^2 \left(A_{rock,SSAV}\right)^2} \qquad (10)$$

274   where $A_{rock,SSAV}$ is the specific surface area of the solid rock per unit volume of the

275   solid rock [m^2/m^3], which depends on the mineral composition of the porous media; C

276   is a coefficient that equals 0.2; and θ_0 is the initial porosity of the medium. The initial

277   estimated permeability values are 2.24×10^{-10} m^2 in the conducting fracture and

278   3.71×10^{-13} m^2 in the rock matrix according to the initial porosities of 0.60 and 0.12 and

279   Eq. (10).

280   Mineral dissolution or precipitation changes the medium's porosity and permeability. The

281   medium's permeability is updated in time and space by using the Kozeny-Carman

282   relationship (Lai et al., 2014; Xu et al., 2014):

283 $$\kappa = \kappa_0 \frac{(1-\theta_0)^2 \theta^3}{(1-\theta)^2 \theta_0^3} \qquad (11)$$

284   *2.9. Sorption of mobile species*

285   Different minerals have shown a capacity to adsorb CO_2 (Santschi and Rossi, 2006; Fujii et

286   al., 2010; Tabrizy et al., 2013; Heller and Zoback, 2014). Santschi and Rossi (2006) reported

287   that dissolved CO_2 adsorbs onto calcite mineral surfaces through the formation of an

288   intermediate species [$Ca(OH)(HCO_3)$], with a partition coefficient of 6.6×10^{-2} m^3/kg. In their

289   experimental study, Fujii et al. (2010) observed the reversible nature of the sorption of CO_2

290   onto rocks and minerals at pressure and temperature conditions that are relevant to CO_2

291   geological storage. Heller and Zoback (2014) observed the lowest CO_2 adsorption capacity for

292   "Eagle Ford 127" clay, which mainly consists of calcite (80%). From their study the values of

293   partition coefficient were deduced as 7.39×10^{-4} m^3/kg and 3.33×10^{-3} m^3/kg for "Eagle Ford

294   127" and "Montney" clay types respectively at a pressure of 105×10^5 Pa.

295   In this study a value of 2.50×10^{-4} m^3/kg was used as a partition coefficient that is lower than

296   the values reported by Santschi and Rossi (2006) and by Heller and Zoback (2014). The

297   reason is that these authors used crushed rock in their experiments, whereas this study deals

298   with intact rock, thus with smaller reactive surface areas. Additionally, we use the same

299   partition coefficient for all the mobile species because of the large uncertainty in the sorption

300   properties and complex geochemical interactions of all the species and to simplify the

301   analysis.

302   *2.10. Initial and boundary values*

303   The initial pressure in the domain is defined as the hydrostatic pressure with a

304   subsurface pressure gradient of 1×10^4 Pa/m (Pruess, 2008). The pressures equal

305   105×10^5 Pa at the bottom and 95×10^5 Pa at the top for this gradient and an atmospheric

306   pressure of 1×10^5 Pa, assuming that the domain is located at a depth of 1040 m below

307   the land surface. In the base-case transport scenarios, an excess pressure of 71.63 Pa in

308   addition to the prevailing hydrostatic pressure is applied at the bottom boundary to

309   obtain fluid Darcy velocities of 10 and 2×10^{-2} m/year in the conducting fracture and

310   rock matrix, respectively. These velocities show a combined Darcy velocity of 0.0202

311   m/year for the fracture plus the matrix system. This velocity falls in the range for

312   regional-scale Darcy velocities of 1 to 10 cm/year, which are measured in a number of

313   sedimentary basins (Bachu et al., 1994).

314   The initial water chemistry in the reservoir and transport domain (clay-rich caprock) is

315   obtained from the background Batch Geochemical Modelling (BGM). The background BGM

316   is performed at a temperature of 45°C and CO_2 partial pressure of 1×10^3 Pa (Xu et al., 2005)

317   and considers 0.5 M of NaCl solution until full equilibrium is reached (with respect to all the

318   reactions in Table 1). The chemistry of the leaking CO_2-saturated brine is obtained from CO_2

319   dissolution modelling that is performed at a temperature of 45°C and CO_2 partial pressure of

320   105×10^5 Pa (representing a depth of 1040 m below the surface) for a 0.5 M NaCl solution.

321 Table 3 displays the initial water chemistry in the reservoir and clay-rich caprock (column 2)

322 and that of the leaking CO_2-saturated brine in the reservoir (column 3). The compositions of

323 the initial and boundary brines in the modelling process, written in terms of chemical

324 components, are presented in Table 4. The composition of leaking brine at the bottom inflow

325 boundary is set to remain constant during the entire simulation time, assuming that the brine

326 in the reservoir always stays in equilibrium with calcite.

327
328 **Table 3.** Initial prevailing water chemistry in the reservoir and clay-rich caprock (column 2)
329 and the chemistry of CO_2-saturated brine in the reservoir (column 3).

Pressure and temperature	45°C and 1×10^3 Pa	45°C and 105×10^5 Pa
Aqueous species	c [mol/(kg water)]	c [mol/(kg water)]
HCO_3^-	3.33×10^{-3}	6.04×10^{-2}
Na^+	4.99×10^{-1}	4.89×10^{-1}
Cl^-	5.00×10^{-1}	5.00×10^{-1}
Ca^{2+}	2.01×10^{-3}	3.58×10^{-2}
CO_{2aq}	1.98×10^{-4}	1.08
H^+	5.44×10^{-8}	1.67×10^{-5}
OH^-	1.29×10^{-6}	4.25×10^{-9}
CO_3^{2-}	1.43×10^{-5}	8.85×10^{-7}
$NaHCO_{3aq}$	6.63×10^{-4}	1.13×10^{-2}
pH	7.26	4.78

330

331 **Table 4**. Initial (sub-index 0) and boundary conditions (sub-index bc) in terms of the chemical
332 components. The translation of aqueous species to component species and viceversa can be
333 seen in Appendix A.

Component species	Concentration [mol/(kg water)]	Component species	Concentration [mol/(kg water)]
$u_{HCO_{3,0}}$	4.02×10^{-3}	$u_{HCO_{3,bc}}$	7.17×10^{-2}
u_{Na_0}	5.00×10^{-1}	$u_{Na_{bc}}$	5.00×10^{-1}
u_{Ca_0}	2.01×10^{-3}	$u_{Ca_{bc}}$	3.58×10^{-2}
$u_{CO_{2,0}}$	1.82×10^{-4}	$u_{CO_{2,bc}}$	1.08

334

16

335   *2.11. Various reactive transport scenarios*

336   Various reactive transport scenarios (Table 5) for leaking CO_2-saturated brine are

337   performed to analyze the effects of different transport processes on the mobility and

338   retention of CO_{2aq}, as well as the variations in the medium's porosity and permeability

339   along the leakage pathway driven by geochemical reactions. The transport modelling

340   of leaking CO_2-saturated brine is performed for a period of 500 years.

341   *2.11.1. Base-case transport scenarios*

342   We denote scenarios 1, 2, 3 and 4 as the base cases, aimed at investigating the roles of

343   advection and dispersion in the rock matrix (advection-dominated transport) compared

344   to diffusion alone (diffusive transport). In all cases, advection, diffusion and dispersion

345   are considered to occur in the fracture. In scenarios 1 and 3, the mass transport in the

346   rock matrix is modelled by considering that the only active transport process is

347   diffusion, while scenarios 2 and 4 include advection and dispersion alongside diffusion

348   in the rock matrix. Sorption is included in scenarios 3 and 4. The longitudinal and

349   transverse dispersivity values for transport scenarios 1 and 3 are 10 m and 1 m,

350   respectively, in the fracture and zero in the rock matrix. The same longitudinal and

351   transverse dispersivity values are used in transport scenarios 2 and 4, but now both in

352   the fracture and the rock matrix. The dispersivity values are related to the length scale

353   of the transport domain, as reported by Gelhar et al. (1992).

354

355

356

357

358   Table 5. Various base-case reactive transport scenarios (1, 2, 3 and 4) and the reactive
359   transport scenarios (5, 6, 7 and 8) in the sensitivity analysis.

Reactive transport scenario	Partition coefficient [m^3/kg]	Initial velocity [m/year]	Longitudinal dispersivity in fracture / matrix [m]	Advection in the matrix	Excess pressure at the bottom [Pa]
1	0	10	10 / 0	N	71.625
2	0	10	10 / 10	Y	71.625
3	2.5×10^{-4}	10	10 / 0	N	71.625
4	2.5×10^{-4}	10	10 / 10	Y	71.625
5	0	5	10 / 10	Y	20.750
6	0	15	10 / 10	Y	122.50
7	0	10	20 / 20	Y	71.625
8	0	10	30 / 30	Y	71.625

360

2.11.2. Sensitivity analysis

362   Sensitivity analysis is performed to investigate the roles of fluid velocity and

363   dispersivity on the reactive transport of CO_{2aq} along the leakage pathway. Thus, we

364   perform additional reactive transport scenarios 5, 6, 7 and 8 (Table 5). Scenarios 5 and

365   6 involve, respectively, maximum fluid velocities of nearly 5 m/year and 15 m/year at

366   the bottom (inlet) of the fracture, matching the regional-scale Darcy velocities that are

367   characteristic of deep sedimentary basins (Bachu et al., 1994). These velocities are achieved

368   by applying an excess pressure of 20.75 Pa and 122.50 Pa, respectively, in addition to the

369   prevailing hydrostatic pressure at the bottom boundary. Pressures are kept constant in time, so

370   that velocities vary in space and time driven by changes in porosity and permeability caused

371   by mineral reaction. The longitudinal dispersivity values in scenarios 7 and 8 are 20 m

372   and 30 m, respectively, in both the fracture and the rock matrix. A transverse

373   dispersivity of 1 m is used in both the fracture and the rock matrix for transport

374   scenarios 5 to 8 (sensitivity not tested).

375   *2.12. Methodology of calculating the mass conversion of CO$_{2aq}$ in geochemical reactions*

376   The mass conversion of CO$_{2aq}$ in geochemical reactions in each reactive transport

377   scenario (Table 5) is calculated by comparing the mass balances with those from

378   conservative transport scenarios (thus neglecting all the geochemical reactions in Table

379   1). The mass balance of CO$_{2aq}$ in each scenario is calculated by considering the

380   cumulative mass that enters the transport domain through the bottom inflow boundary,

381   the mass that leaves through the top open boundary, and the mass that is stored in the

382   aqueous and adsorbed states in the transport domain over time. The mass conversion of

383   CO$_{2aq}$ in geochemical reactions is presented in each reactive transport scenario as a

384   percentage of the mass inflow as $\% \, m_{con} = \frac{m_{con}}{m_{in}} 100$, that is, the ratio between the

385   cumulative mass conversion of CO$_{2aq}$ in geochemical reactions (m_{con}) and its

386   cumulative mass inflow (m_{in}) over time.

387   *2.13. Numerical solution technique*

388   The reactive transport coupled system of equations ((1)-(11)) with the corresponding

389   initial and boundary conditions is modelled in COMSOL Multiphysics®. The flow and

390   transport are modelled by adopting a one-domain approach with a single set of

391   transport equations for the entire domain (fracture plus rock matrix) (Goyeau et al.,

392   2003; Jamet et al., 2009; Tao et al., 2013; Basirat et al., 2015). In this study, we solve

393   the non-linear system of equations that arises from coupled reactive transport

394   modelling by using a segregated approach, which sequentially solves the various

395   physics that are involved. Thus, the solution includes segregated solution steps with

396   individual custom damping and tolerance. A damped version of Newton's method is

397   used in all steps, with damping factors that equal unity. The flow problem (pressure

398   and velocity field) is solved first (segregated step 1), the transport problem for

399   conservative species (components) is next (step 2), followed by the speciation problem

400   (finding the aqueous species as a function of transport component species) in step 3;

401   finally, the mass conservation equation of kinetic mineral calcite is solved in step 4. An

402   implicit non-linear solver that is based on the backward differentiation formula (BDF)

403   is used for time marching. The Jacobian matrix is updated every iteration to make the

404   solver more stable. A structured mesh with quadrilateral elements is used as the

405   numerical grid in the transport domain (fracture plus rock matrix). The mesh is refined

406   in and near the fracture and towards the bottom inlet boundary (supplementary

407   material). The complete mesh consists of 16560 quadrilateral elements. A total of

408   269509 degrees of freedom (DOF) are solved. The average time for solving each of the

409   reactive transport scenarios is nearly 12 hours on an Intel(R) Core(TM)2 Quad CPU

410   with RAM of 16 GB.

411   **3. Results**

412   The mixing of leaking CO_2-saturated brine with the resident pore waters in the

413   transport domain (both the fracture and rock matrix in the clay-rich caprock) created a

414   fluid under-saturated with respect to calcite, thus initiating calcite dissolution near the

415   bottom inflow boundary. Calcite within the transport domain might dissolve or

416   precipitate depending on the evolving geochemical conditions during the simulation.

417   *3.1. Base-case reactive transport scenarios*

418   The calcite dissolution and precipitation reactions, which are driven by leaking CO_2-

419   saturated brine, caused variations in the medium's porosity and permeability in space

420   and time along the transport pathway. Fig. 2a and 2b show the variations in the

421   porosity and permeability in the rock matrix for the reactive transport scenario 2 after a

422   simulation time of 500 years. The rock matrix's porosity increased by nearly 42% from

423   the initial value of 0.12 to a value of 0.17, whereas the permeability attained a value of

424   1.337×10^{-12} m^2 from its initial value of 3.71×10^{-13} m^2. This increase was mostly

425   concentrated near the bottom inflow boundary because of continued calcite dissolution,

426   which was driven by leaking CO_2-saturated brine. A negligible decrease in porosity

427   and permeability was observed towards the top of the transport domain along the

428   conducting fracture, which indicates a small amount of calcite precipitation.
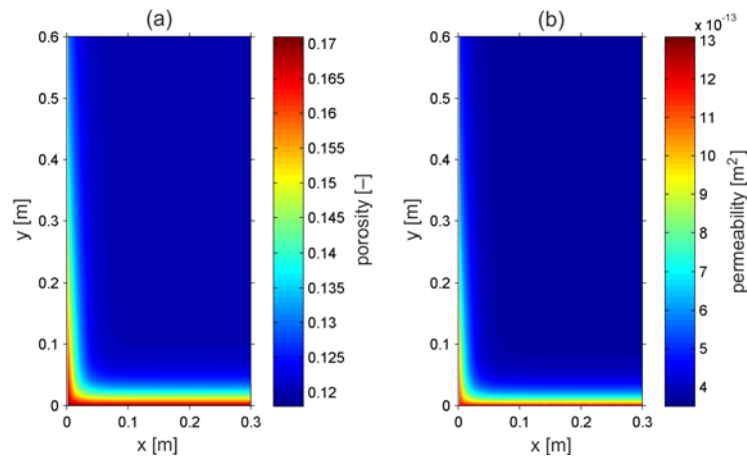
430   Figure 2. Variations in the porosity (a) and permeability (b) of the rock matrix in the base-
431   case reactive transport scenario 2 after 500 years.
432

433   *3.1.1. Role of advection and dispersion in the rock matrix*

434   Figs. 3, 4 and 5 present the mass of CO_{2aq} that entered the transport domain from the reservoir

435   through the inflow boundary, its mass conversion in geochemical reactions and percent mass

436   conversion, respectively, in the various studied reactive transport scenarios. In the advection-

437   dominated transport scenarios 2 and 4, the combination of advection, dispersion and diffusion

438   transport processes increased the leakage of CO_{2aq} from the reservoir (Fig. 3a, 3b) and mass

439   conversion during the geochemical reactions (Fig. 4a, 4b) along the transport domain

440   compared to the corresponding values in diffusive transport scenarios 1 and 3.

21

441   The mass balances of CO_{2aq} in the transport domain in the base-case reactive transport

442   scenarios 1, 2, 3 and 4 after 500 years are reported in Table 6. This table lists the CO_{2aq} mass

443   inflows from the reservoir, the mass that was stored in aqueous and adsorbed states, the mass

444   that was converted in geochemical reactions, and the mass that left the transport domain

445   through the top open boundary.
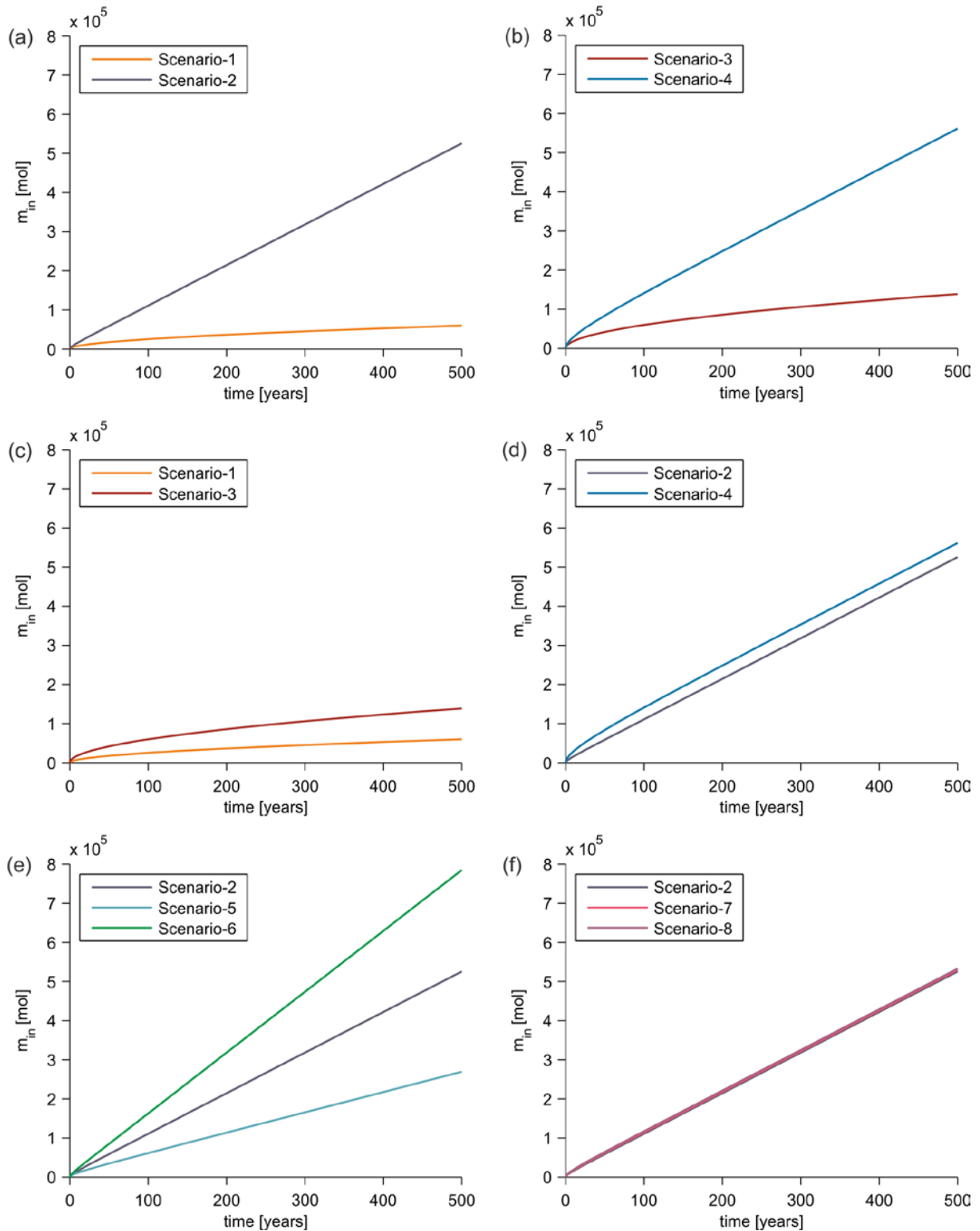
446

447 Figure 3. Mass inflow of CO_{2aq} through the bottom inflow boundary in various reactive
448 transport scenarios over time: (a) scenarios 1 and 2; (b) scenarios 3 and 4; (c) scenarios 1 and
449 3; (d) scenarios 2 and 4; (e) scenarios 2, 5 and 6; and (f) scenarios 2, 7 and 8.
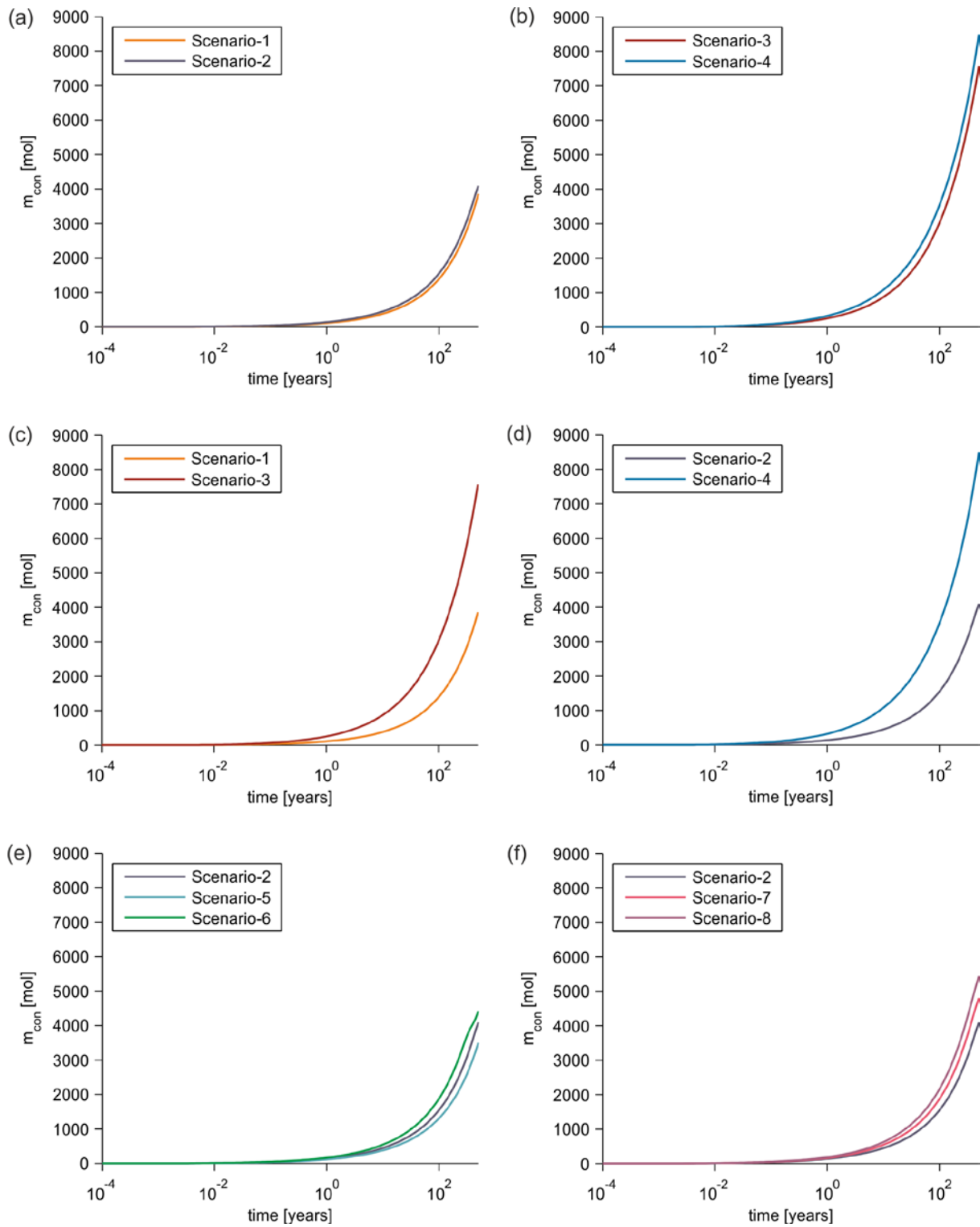
Figure 4. Mass conversion of CO_{2aq} in various reactive transport scenarios over time: (a) scenarios 1 and 2; (b) scenarios 3 and 4; (c) scenarios 1 and 3; (d) scenarios 2 and 4; (e) scenarios 2, 5 and 6; and (f) scenarios 2, 7 and 8.
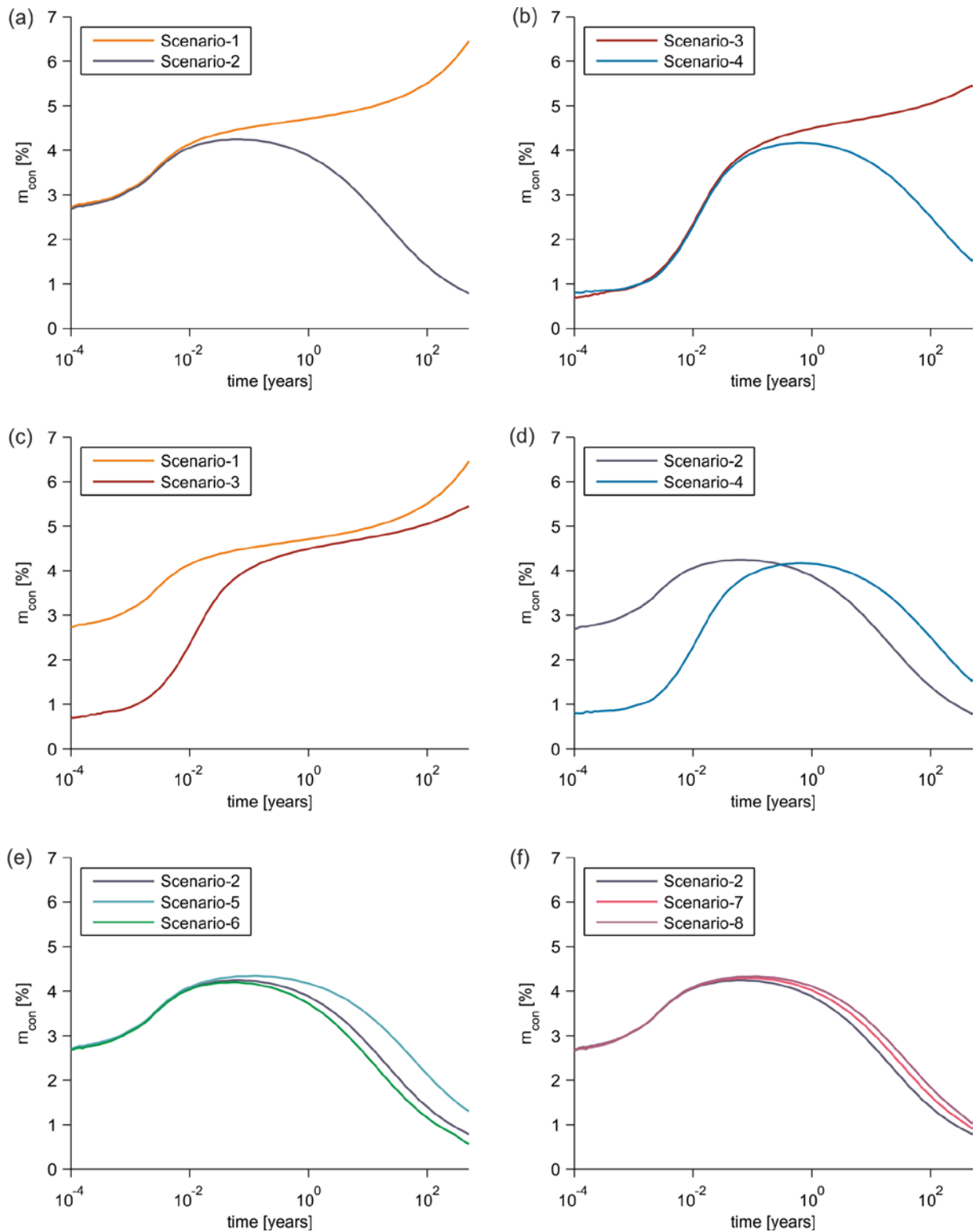
Figure 5. Percentage mass conversion of CO_{2aq} in various reactive transport scenarios over time; (a) scenarios 1 and 2; (b) scenarios 3 and 4; (c) scenarios 1 and 3; (d) scenarios 2 and 4; (e) scenarios 2, 5 and 6; and (f) scenarios 2, 7 and 8.

459   The total mass inflow was split in terms of advective, dispersive and diffusive fluxes

460   through the bottom inflow boundary both at the fracture and in the rock matrix. The

461   highest mass inflow, mass that was stored in an aqueous state and mass conversion of

462   CO_{2aq} were associated with the advection-dominated transport scenarios 2 and 4

463   compared to the values in the corresponding diffusive transport scenarios 1 and 3.

464   Higher stored mass in an adsorbed state can also be observed in the advection-

465   dominated transport scenario 4 compared to the corresponding diffusive transport

466   scenario 3. The mass balance errors were less than 0.1% in all the scenarios.

467   **Table 6.** CO_{2aq} mass balance [mol] in the base-case reactive transport scenarios 1, 2, 3, and 4
468   after 500 years.

Reactive transport scenarios	Scenario 1	Scenario 2	Scenario 3	Scenario 4
Total mass that entered the domain	5.98×10^4	5.26×10^5	1.39×10^5	5.62×10^5
Mass that entered from advection (fracture)	5.70×10^3	5.56×10^3	6.04×10^3	5.78×10^3
Mass that entered from diffusion (fracture)	1.79×10^0	2.94×10^{-1}	3.85×10^0	1.68×10^0
Mass that entered from dispersion (fracture)	3.19×10^3	5.12×10^2	7.21×10^3	3.02×10^3
Mass that entered from advection (matrix)	0	5.12×10^5	0	5.12×10^5
Mass that entered from diffusion (matrix)	5.09×10^4	4.86×10^3	1.26×10^5	2.49×10^4
Mass that entered from dispersion (matrix)	0	3.12×10^3	0	1.60×10^4
Mass that left the domain (fracture)	9.24×10^{-1}	1.69×10^2	9.14×10^{-1}	9.14×10^{-1}
Mass that left the domain (matrix)	0.00×10^0	3.32×10^3	0.00×10^0	8.65×10^1
Mass stored in an aqueous state	5.59×10^4	5.19×10^5	2.22×10^4	9.31×10^4
Mass stored in an adsorbed state	0.00×10^0	0.00×10^0	1.09×10^5	4.60×10^5
Mass converted in the geochemical reactions	3.86×10^3	4.09×10^3	7.57×10^3	8.49×10^3
Mass conversion of CO_{2aq} after 500 years (%)	6.46×10^0	7.79×10^{-1}	5.45×10^0	1.51×10^0
Error in the mass balance (%)	1.82×10^{-2}	-9.16×10^{-2}	1.97×10^{-2}	1.34×10^{-2}

469

470   The mass balance for mineral calcite and Ca^{2+} and the split for the mass of calcite [mol] and

471   pore volume [m^3] in the fracture and rock matrix in the base-case transport scenarios 1, 2, 3

472   and 4 after 500 years are presented in Table 7. Calcite dissolution prevailed over precipitation

473   in the transport domain during the simulations, which implies a decrease in its mass and

474   increase in the overall pore volume in the fracture and rock matrix. Considering advection in

475   the rock matrix (scenarios 2 and 4) increased the calcite dissolution, pore volume and mass of

476   Ca^{2+} compared to the corresponding diffusive transport scenarios 1 and 3. Moreover,

477   relatively higher calcite dissolution occurred in the fracture than in the rock matrix compared

478   to the initial mass of calcite in the fracture and rock matrix because of the higher advective

479   velocity in the former. Finally, the mass of produced Ca^{2+} was equal to the mass of dissolved

480   calcite (except for the mass balance errors of less than 0.14%).

481   **Table 7**. Mass balance [mol] of calcite and Ca^{2+} and increase in the pore volume [m^3] in the
482   transport domain for the base-case reactive transport scenarios (1, 2, 3, and 4) after 500 years.

Reactive transport scenarios	Scenario 1	Scenario 2	Scenario 3	Scenario 4
Mass of dissolved calcite in the fracture	7.26×10^0	7.33×10^0	1.24×10^1	1.36×10^1
Decrease in mass in the fracture (%)	2.31×10^0	2.33×10^0	3.94×10^0	4.33×10^0
Mass of dissolved calcite in the rock matrix	3.81×10^3	4.07×10^3	7.58×10^3	8.36×10^3
Decrease in mass in the rock matrix (%)	1.10×10^{-2}	1.18×10^{-2}	2.19×10^{-2}	2.42×10^{-2}
Total mass of dissolved calcite	3.81×10^3	4.08×10^3	7.59×10^3	8.38×10^3
Increase in pore volume in the fracture	2.68×10^{-4}	2.71×10^{-4}	4.57×10^{-4}	5.02×10^{-4}
Increase in pore volume in the rock matrix	1.41×10^{-1}	1.50×10^{-1}	2.80×10^{-1}	3.09×10^{-1}
Total increase in the pore volume	1.41×10^{-1}	1.51×10^{-1}	2.80×10^{-1}	3.09×10^{-1}
Mass of produced Ca^{2+}	3.81×10^3	4.08×10^3	7.58×10^3	8.37×10^3
Error in the mass balance (%)	-1.03×10^{-1}	-4.75×10^{-2}	1.42×10^{-1}	4.40×10^{-2}

483

484   Sorption in the transport scenarios 3 and 4 increased the CO_{2aq} leakage from the reservoir

485   (Fig. 3c, 3d) and mass conversion of CO_{2aq} in the geochemical reactions (Fig. 4c, 4d) in the

486   transport domain compared to the transport scenarios 1 and 2, which did not consider

487   sorption. Comparing the sorption scenario-3 with the corresponding no-sorption scenario 1

488   and the sorption scenario 4 with the no-sorption scenario 2 indicates that sorption almost

489   doubled the mass conversion of CO_{2aq} in the geochemical reactions (row 13 of Table 6);

490   calcite dissolution (row 6 of Table 7), with an associated increase in pore volume (row 9 of

491   Table 7); and production of Ca^{2+} (row 10 of Table 7).

492   Although the advection-dominated transport scenarios 2 and 4 increased the conversion of

493   CO_{2aq} mass [mol] in the geochemical reactions compared to the corresponding diffusive

494   transport scenarios 1 and 3, decreasing trends in the percentage mass conversion were

495   observed (Fig. 4a vs Fig. 5a and Fig. 4b vs Fig. 5b). Similarly, higher CO_{2aq} mass conversion

496   occurred in the sorption transport scenarios 3 and 4 compared to the corresponding no-

497   sorption transport scenarios 1 and 2, yet decreasing trends were observed for the percent mass

498   conversion in these scenarios (Fig. 4c vs Fig. 5c and Fig. 4d vs Fig. 5d). This result can be

499   explained by the variability in the CO_{2aq} mass inflows.

500   *3.2. Sensitivity analysis*

501   *3.2.1. Role of velocity magnitude*

502   Different initial fluid velocities prevailed in the fracture and rock matrix because of different

503   excess pressure at the bottom boundary of the transport domain in scenarios 2, 5, and 6;

504   velocities then changed during the simulation time due to variations in porosity and

505   permeability. Mass inflows (Fig. 3e) and CO_{2aq} mass conversion in the reactions (Fig. 4e)

506   increased with the initial fluid velocity in the transport pathway. However, the percentage of

507   mass conversion of CO_{2aq} decreased with increasing fluid velocity (Fig. 5e). The mass

508   conservation indicated that the mass inflow and mass conversion of CO_{2aq} in the geochemical

509   reactions increased with increasing fluid velocity in the transport domain (Table 6 and 8).

510   Additionally, the mass of dissolved calcite, the pore volume and the mass production of Ca^{2+}

511   increased with increasing fluid velocity in scenarios 2, 5 and 6.

512

513 **Table 8**. CO_{2aq} mass balance [mol] for the different reactive transport scenarios 5, 6, 7, and 8
514 after 500 years.

Reactive transport scenarios	Scenario 5	Scenario 6	Scenario 7	Scenario 8
Total mass that entered the domain	2.69×10^5	7.85×10^5	5.29×10^5	5.33×10^5
Mass that entered from advection (fracture)	2.77×10^3	8.31×10^3	5.60×10^3	5.61×10^3
Mass that entered from diffusion (fracture)	6.23×10^{-1}	1.89×10^{-1}	3.14×10^{-1}	3.24×10^{-1}
Mass that entered from dispersion (fracture)	5.42×10^2	4.95×10^2	1.10×10^3	1.70×10^3
Mass that entered from advection (matrix)	2.55×10^5	7.68×10^5	5.12×10^5	5.12×10^5
Mass that entered from diffusion (matrix)	9.03×10^3	3.38×10^3	4.75×10^3	4.68×10^3
Mass that entered from dispersion (matrix)	1.45×10^3	4.85×10^3	6.11×10^3	9.04×10^3
Mass that left the domain (fracture)	4.74×10^{-1}	2.03×10^3	2.92×10^2	4.03×10^2
Mass that left the domain (matrix)	4.32×10^1	1.35×10^5	6.26×10^3	9.40×10^3
Mass stored in an aqueous state	2.66×10^5	6.42×10^5	5.18×10^5	5.18×10^5
Mass stored in an adsorbed state	0	0	0	0
Mass converted in the geochemical reactions	3.50×10^3	4.42×10^3	4.81×10^3	5.43×10^3
Mass conversion of CO_{2aq} after 500 years (%)	1.30×10^0	5.63×10^{-1}	9.10×10^{-1}	1.02×10^0
Error in the mass balance (%)	5.47×10^{-3}	4.83×10^{-2}	-1.01×10^{-1}	-1.03×10^{-1}

515
516 **Table 9**. Mass balance [mol] of calcite and Ca^{2+} and increase in the pore volume [m^3] in the
517 transport domain for the different transport scenarios 5, 6, 7, and 8 after 500 years.

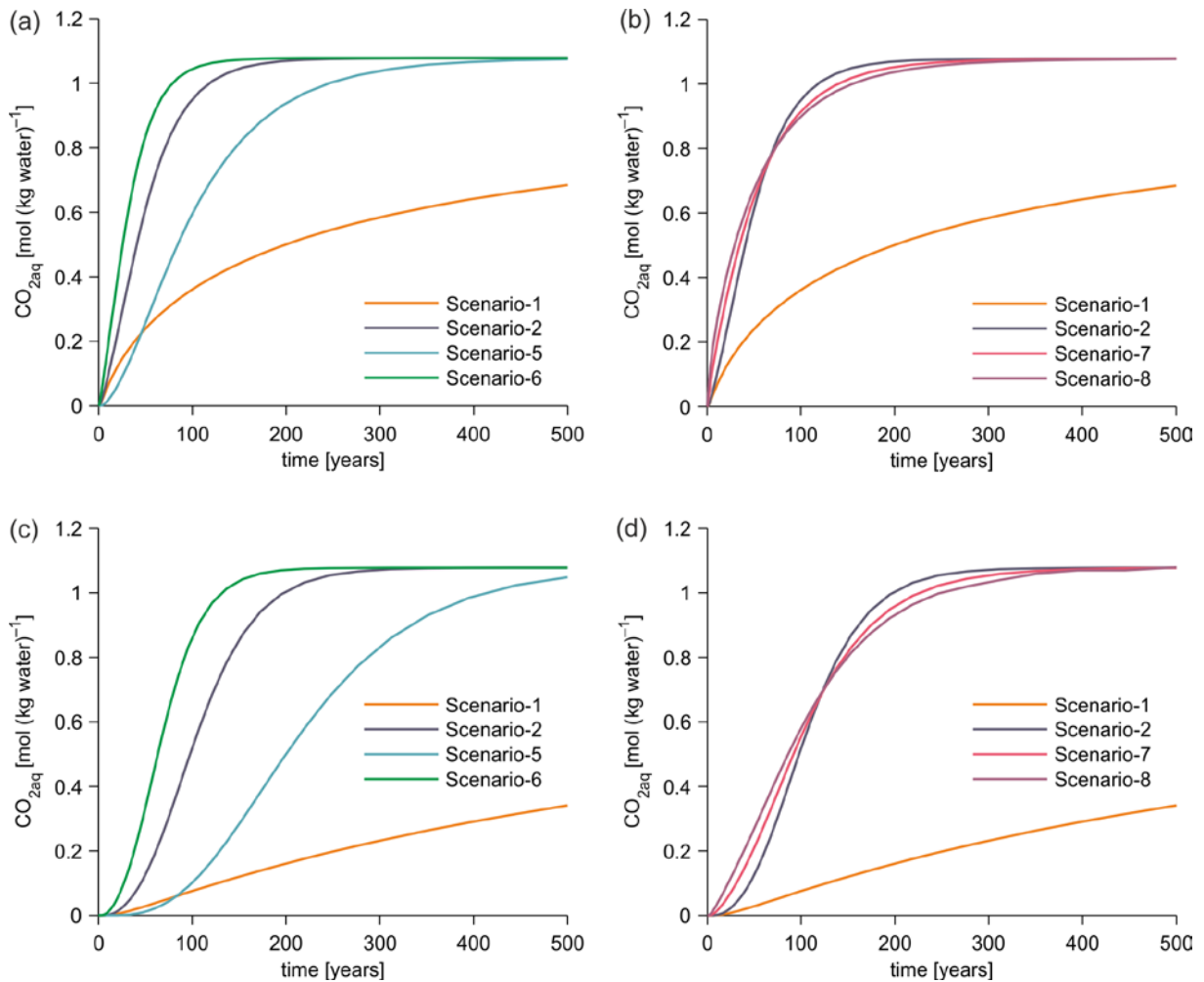| Reactive transport scenarios	Scenario 5	Scenario 6	Scenario 7	Scenario 8
Mass of dissolved calcite in the fracture	4.65×10^0	4.88×10^0	7.43×10^0	8.54×10^0
Decrease in mass in the fracture (%)	1.48×10^0	1.55×10^0	2.36×10^0	2.72×10^0
Mass of dissolved calcite in the rock matrix	3.48×10^3	4.43×10^3	4.80×10^3	5.40×10^3
Decrease in mass in the rock zone	1.01×10^{-2}	1.28×10^{-2}	1.39×10^{-2}	1.56×10^{-2}
Total mass of dissolved calcite	3.49×10^3	4.43×10^3	4.80×10^3	5.41×10^3
Increase in pore volume in the fracture	1.72×10^{-4}	1.80×10^{-4}	2.74×10^{-4}	3.15×10^{-4}
Increase in pore volume in the rock matrix	1.29×10^{-1}	1.63×10^{-1}	1.77×10^{-1}	1.99×10^{-1}
Total increase in the pore volume	1.29×10^{-1}	1.64×10^{-1}	1.77×10^{-1}	2.00×10^{-1}
Mass of produced Ca^{2+}	3.49×10^3	4.43×10^3	4.81×10^3	5.41×10^3
Error in the mass balance (%)	6.16×10^{-3}	5.32×10^{-2}	-1.07×10^{-1}	-1.13×10^{-1}

518

519

3.2.2. Role of longitudinal dispersivity

The higher longitudinal dispersivity very slightly increased the mass inflow (5.26×10^5, 5.29×10^5 and 5.33×10^5 mol in scenarios 2, 7 and 8, respectively) (Figs. 3f and 4f; Tables 6 and 8). However, the mass conversion of CO_{2aq} in the geochemical reactions (Fig. 4f) and percent mass conversion (Fig. 5f) increased with increasing dispersivity. In these scenarios, the higher quantities of CO_{2aq} that were converted in the geochemical reactions for almost the same mass inflows resulted in similar trends for CO_{2aq} mass conversion and its percentage of mass conversion (Figs. 4f and 5f; Table 8). For a given fluid velocity, the mass of dissolved calcite, the mass of produced Ca^{2+}, and the pore volume increased with the longitudinal dispersivity (Tables 7 and 9).

3.3. Breakthrough curves of leaking CO_{2aq}

The effects of advection and dispersion in the rock matrix on the transport of leaking CO_{2aq} are presented in the form of breakthrough curves, which represent its concentration at 10 and 20 m locations from the bottom inlet boundary along the conducting fracture over time (Fig. 6). Fast migration of CO_{2aq} along the leakage pathway was observed in the advection-dominated transport scenarios compared to the diffusive transport scenarios. Fast transport that was mainly driven by advection increased the CO_{2aq} concentration in the advection-dominated transport scenario 2 compared to the diffusive transport scenario 1 after a travel distance of 10 and 20 m along the conducting fracture. Additionally, the highest velocity in scenario 6 resulted in the highest concentration of CO_{2aq} (Fig. 6a and 6c). During earlier times, the higher dispersivity in scenario 8 increased the concentration of CO_{2aq} (Fig. 6b and 6d). However, the lowest dispersivity value used in scenario 2 resulted in the highest CO_{2aq} concentration after 67 and 135 years for the 10- and 20-m locations, respectively. This result

543   occurred because of the fast spreading and dilution of species concentration that was caused

544   by higher dispersion along the transport pathway over time in scenario 8.

545

546   Figure 6. Breakthrough curves for CO_{2aq} for various reactive transport scenarios at various
547   locations along the fracture over time; (a) scenarios 1, 2, 5, and 6 at 10 m from the inflow
548   boundary; (b) scenarios 1, 2, 7, and 8 at 10 m; (c) scenarios 1, 2, 5, and 6 at 20 m from the
549   inflow boundary; and (d) scenarios 1, 2, 7, and 8 at 20 m.
550

551   **4. Discussion**

552   The role of calcite kinetics in contact with CO2-saturated brine in the reservoir in the presence

553   of free-phase CO2 in the reservoir has been investigated. For the purpose, two sets of CO_2

554   dissolution modelling have been performed for elevated values of CO_{2aq} in the presence of

555   free-phase CO_2 in the reservoir for calcite was (i) reactive and (ii) non-reactive. The presence

31

556　　of calcite kinetics provided buffer and kept pH at a higher value of 4.78 whereas pH settled at

557　　3.56 in the absence of calcite reaction. This added alkalinity caused by calcite dissolution may

558　　shift CO_{2aq} into other ions in solution along the transport domain. Calcite dissolution in the

559　　reactive transport scenarios mainly occurred in close vicinity to the bottom inflow boundary

560　　(Gherardi et al., 2007; Andreani et al., 2008; Ellis et al., 2011b), resulting in the simultaneous

561　　production of Ca^{2+} and HCO_3^-, which brought the brine solution closer to calcite saturation

562　　away from the inflow boundary. The resulting saturation conditions with respect to calcite

563　　stopped any significant calcite dissolution in the rock matrix beyond 0.1 m from the inflow

564　　boundary, and caused mineral precipitation towards the top of the transport domain, mainly

565　　close to the conducting fracture. However, calcite precipitation was too low to have any

566　　significant effect on the decrease in porosity and permeability in the fracture and rock matrix.

567　　In scenario 6, the rock matrix's porosity attained a value of 0.17 after 500 years at the inflow

568　　boundary but reached a value of 0.15 (the initial one was 0.12) approximately 0.01 m from the

569　　boundary. However, the rock matrix's porosity close to the fracture was higher than 0.15 up

570　　to a distance of 0.25 m from the inflow boundary in scenario 6. This result can be explained

571　　by the fast transport along the fracture, which caused calcite dissolution to occur over a

572　　relatively longer distance.

573　　Declining trends in the percent mass conversion after some initial times that were observed in

574　　Fig. 5d as compared to Fig. 5c, are related to additional advection in the rock matrix in the

575　　advection-dominated transport scenarios 2 and 4. The percent mass conversion in scenarios 2

576　　and 4 fell off after 2.01×10^6 s and 1.89×10^7 s, respectively (Fig. 5a, 5b, and 5d) but continued

577　　to increase in scenarios 1 and 3 (Fig. 5a, 5b, and 5c). Advection in scenarios 2 and 4 increased

578　　the mass inflows at an almost constant rate, whereas the mass inflow decreased with time in

579　　scenarios 1 and 3 due to the decreasing diffusive fluxes across the inflow boundary. Although

580　　the concentration gradients across the inflow boundary kept decreasing over time in all these

581   transport scenarios, the diffusive fluxes were the only transport process across the inflow

582   boundary in the diffusive transport scenarios 1 and 3, which decreased the mass inflow

583   compared to the corresponding inflows in the advection-dominated transport scenarios 2 and

584   4. Thus, the higher mass inflow in scenarios 2 and 4 with time created declining trends in

585   percent mass conversion (Fig. 5a, 5b, and 5d).

586   The higher observed mass conversion of CO_{2aq} in the geochemical reactions in sorption

587   scenarios 3 and 4 compared to the corresponding no-sorption scenarios 1 and 2 (Fig. 4c and

588   4d) were mainly related to (i) the higher mass inflows through the inflow boundary induced

589   by sorption and, to a lesser extent, (ii) the lower saturation state of calcite in the transport

590   domain when sorption was included in the simulations. Over time, relatively lower saturation

591   of calcite (mineral) prevailed in the transport domain in the sorption scenarios 3 and 4

592   compared to the no-sorption scenarios 1 and 2. The sorption process fixed the mass of Ca^{2+}

593   and HCO_3^- onto the rock surfaces and lowered the concentration of these species in an

594   aqueous state. This process lowered the saturation state of calcite in the sorption scenarios 3

595   and 4, promoting calcite dissolution and thus contributing towards the overall higher CO_{2aq}

596   mass conversion in the geochemical reactions in these scenarios.

597   Higher percent mass conversion occurred during earlier times in the no-sorption scenarios 1

598   and 2 compared to the corresponding sorption scenarios 3 and 4 (Fig. 5c and 5d). This result

599   mainly occurred because sorption (scenarios 3 and 4) induced relatively higher concentration

600   gradients across the inflow boundary; thus, higher diffusive fluxes resulted in higher mass

601   inflows. Sorption fixed the species' masses in an adsorbed state and reduced their

602   concentrations in an aqueous state, increasing the concentration gradients and mass inflows

603   and decreasing the percent mass conversion during these earlier times.

604   This study shows that pH distribution along the transport pathway alone cannot fully predict

605   the calcite reaction kinetics and the related conversion of CO_{2aq} into other ions; instead the

606   reactive process is mostly controlled by the saturation state of calcite. As an example, at a pH

607   of 7.26, the brine was at saturation with respect to calcite and thus no reaction occurred in the

608   transport domain before leakage of CO_2-saturated brine started taking place. On the other

609   hand, leaking CO_2-saturated brine was at a pH of 4.78, and also saturated with respect to

610   calcite, so again no reaction was driven. It was only the mixing of the two fluids (one

611   prevailing in the transport pathway and the other one leaking from the reservoir) that brought

612   the saturation state of calcite below one and caused calcite dissolution, concentrated initially

613   in the vicinity of the lower leaking boundary. Over time, the calcite reaction zone advanced in

614   the transport domain; however, due to the increase in Ca^{+2} and HCO_3^- as a result of calcite

615   dissolution, the saturation state started increasing away from the lower leaking boundary.

616   Eventually geochemical conditions evolved when saturation state with respect to calcite

617   reached one; as a consequence, calcite dissolution ceased even though the pH value was 4.78

618   (representing leaking CO_2-saturated brine), much lower than the initial value of 7.26

619   prevailing in the transport pathway. This shows that the fall in the pH value along the

620   transport pathway did not fully predict the calcite reaction regimes; instead calcite reactivity

621   and related conversion of CO_{2aq} was found related to saturation state of calcite in the transport

622   domain for the modelled leakage scenarios.

623   We computed the saturation state of calcite in the full domain (fracture plus rock matrix) in

624   the no-sorption scenarios 1 and 2 and the corresponding sorption scenarios 3 and 4 over a

625   simulation time of 500 years to further illustrate the role of sorption in maintaining a

626   relatively lower saturation state of calcite, inducing dissolution. The saturation state of calcite

627   was computed as its integral over the entire domain and simulation time. Fig. 7 presents the

628   difference of the saturation state of calcite between the sorption scenarios and the

629   corresponding no-sorption scenarios. Except for the very early times (2.34×10^{-3} year), the

630   saturation state of calcite remained lower in the sorption scenarios 3 and 4 compared to the

631   corresponding no-sorption scenarios 1 and 2. The resulting low saturation state of calcite from

632   sorption increased the conversion of CO_2 through the higher dissolution of calcite.

633
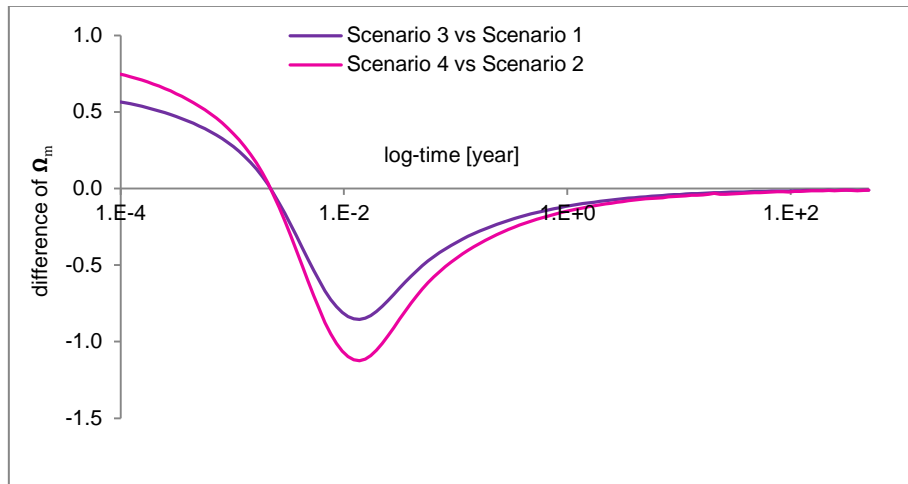
Figure 7. Difference of the saturation state of calcite ($\mathbf{\Omega}_m$) in the transport domain over time:
between the sorption scenario 3 and the corresponding no-sorption scenario1; and between the
sorption scenario 4 and the corresponding no-sorption scenario 2.

637

638   The steep observed gradients of the percent mass conversion of CO_{2aq} during the early times

639   in all the reactive transport scenarios are related to the prevailing higher calcite dissolution

640   reaction rate and associated higher mass conversion of CO_{2aq} relative to the mass inflow

641   through the bottom inflow boundary. During the earlier times, leaking CO_2-saturated brine

642   induced the lowest saturation of calcite and, thus, the highest calcite dissolution reaction rate

643   and CO_{2aq} mass conversion. Furthermore, the mass conversion of CO_{2aq} in the geochemical

644   reactions for all the reactive transport scenarios was well correlated with the calcite

645   dissolution and associated increase in pore volume in the transport domain over time (Fig. 4

646   vs Fig. 8).
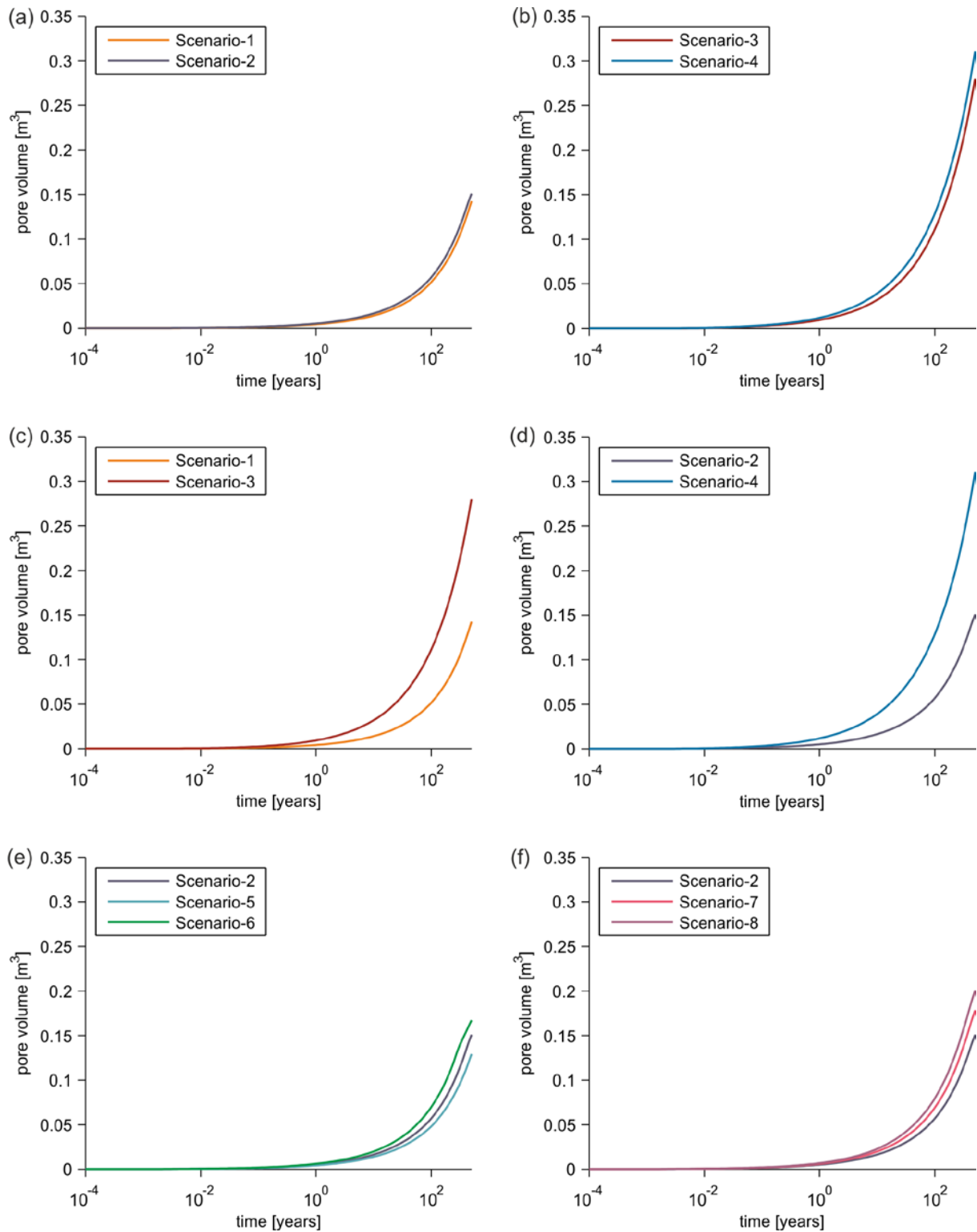
647

648 Figure 8. Increase in pore volume within the transport domain from calcite dissolution in
649 various reactive transport scenarios over time: (a) scenarios 1 and 2; (b) scenarios 3 and 4; (c)
650 scenarios 1 and 3; (d) scenarios 2 and 4; (e) scenarios 2, 5 and 6; and (f) scenarios 2, 7 and 8.
651

652   For the same initial fluid velocity at the bottom boundary of the fracture, the highest CO_{2aq}

653   concentration along the fracture in the advection-dominated transport scenario 2 indicates

654   lower mass transfer from the conducting fracture into the rock matrix, when compared to that

655   in the diffusive transport scenario 1 (Fig. 6a, 6b). The fast transport of CO_{2aq} from advection

656   in the rock matrix in the advection-dominated transport scenario 2 created low concentration

657   gradients across the fracture-matrix interface that, in turn, decreased the diffusive mass

658   transfer from the conducting fracture into the rock matrix.

5. Conclusions

660   This work presents the results of reactive transport simulations of CO_2-saturated brine

661   that leaks along a conducting fracture and a surrounding rock matrix in clay-rich

662   caprock. The model that was developed here considered the effects of advection,

663   dispersion and diffusion in both the fracture and rock matrix on the quantities of leaked

664   CO_{2aq}, the evolution of the medium's porosity and permeability because of

665   geochemical reactions, and the conversion of CO_{2aq} in geochemical reactions along the

666   leakage pathway.

667   Advection and dispersion in addition to diffusion in the rock matrix increased the

668   leakage of CO_{2aq} from the reservoir and its transport speed along the leakage pathway

669   (arriving faster and further) as compared to the scenarios where transport occurred only

670   by diffusion in the rock matrix. The amount of CO_{2aq} that leaked from the reservoir

671   was also found to increase with fluid velocity along the leakage pathway. The mass

672   conversion of CO_{2aq} in the geochemical reactions was found to increase with the fluid

673   velocity and dispersion for the same set of hydraulic and geochemical parameters. The

674   observed increase in CO_{2aq} leakage from the reservoir and the amount that was

675   consumed in the geochemical reactions implies that advection and dispersion in the

676   rock matrix are important transport processes that must be considered in addition to

677   diffusion when modelling the leakage of CO_{2aq} along a fractured pathway.

678

685

686   **APPENDIX**

687   **Appendix A: Writing the chemical component species from the aqueous species involved**

688   **in the equilibrium and mineral kinetic reactions for the reactive transport system**

689   A total of eight aqueous species (HCO_3^-, Na^+, CO_{2aq}, Ca^{2+}, H^+, OH^-, CO_3^{2-}, and $NaHCO_{3aq}$)

690   are involved in four of the equilibrium reactions (R1) to (R4) and the mineral kinetic reaction

691   (R5), which are presented in Table 1. Following the formulation by Saaltink et al. (1998),

692   these eight aqueous species can be converted into four chemical components and written in

693   vector form: $\mathbf{u}^T = \left(u_{HCO3}, \quad u_{Na}, \quad u_{CO2}, \quad u_{Ca} \right)^T$, with the components defined as

694

$$
\begin{cases}
u_{HCO3} = c_{HCO_3^-} - c_{H^+} + c_{OH^-} + 2c_{CO_3^{2-}} + c_{NaHCO_{3aq}} \\
u_{Na} = c_{Na^+} + c_{NaHCO_{3aq}} \\
u_{CO2} = c_{CO_{2aq}} + c_{H^+} - c_{OH^-} - c_{CO_3^{2-}} \\
u_{Ca} = c_{Ca^{2+}}
\end{cases}
\tag{A.1}
$$

695   By transforming all the aqueous species in the reactions into the component species,

696   the required number of transport equations decreases to four (number of chemical

697   component species) from the original eight (number of aqueous species). The

698   source/sink term in transport equation (1) takes the following form:

699
$$\mathbf{r_{kin}} = \begin{cases} r_{u_{HCO_3}} = 2r_m \\ r_{u_{Na}} = 0 \\ r_{u_{CO_2}} = -r_m \\ r_{u_{Ca}} = r_m \end{cases} \tag{A.2}$$

700   Thus, the source/sink term ($\mathbf{r_{kin}}$) provides information regarding the changes in the chemical

701   component species that are driven by the combined effects of equilibrium and mineral kinetic

702   reactions in the reactive transport equation (1). The term (r_m) represents the kinetic reaction

703   (dissolution or precipitation) of mineral calcite, which was defined in equation (4). From

704   (A.2) it is immediately seen that $\mathbf{r_{kin}}$ is only a function of the kinetic reaction; this means

705   that components are independent of the equilibrium reaction (which is actually the

706   definition).

707   **A.2 Speciation modelling**

708   The transport of component species by equation (1) requires calculating the aqueous species

709   concentration at every node of the computational domain. The concentration of aqueous

710   species is obtained from the solution of the following eight algebraic equations (A.3 through

711   A.10), which result from four of the equilibrium reactions (R1) to (R4) and the mineral kinetic

712   reaction (R5):

713
$$\left(c_{H^+} \gamma_{H^+} c_{HCO_3^-} \gamma_{HCO_3^-} \right) - \left(c_{CO_{2aq}} \gamma_{CO_{2aq}} K_{CO_{2aq}} \right) = 0 \tag{A.3}$$

714
$$\left(c_{H^+} \gamma_{H^+} c_{OH^-} \gamma_{OH^-} \right) - \left(K_{H_2O} \right) = 0 \qquad (A.4)$$

715
$$\left(c_{H^+} \gamma_{H^+} c_{CO_3^{2-}} \gamma_{CO_3^{2-}} \right) - \left(c_{HCO_3^-} \gamma_{HCO_3^-} K_{HCO_3^-} \right) = 0 \qquad (A.5)$$

716
$$\left(c_{NaHCO_3aq} \gamma_{NaHCO_3aq} \right) - \left(c_{Na^+} \gamma_{Na^+} c_{HCO_3^-} \gamma_{HCO_3^-} K_{Na^+} \right) = 0 \qquad (A.6)$$

717
$$u_{HCO_3} - \left(c_{HCO_3^-} - c_{H^+} + c_{OH^-} + 2c_{CO_3^{2-}} + c_{NaHCO_3aq} \right) = 0 \qquad (A.7)$$

718
$$u_{Na} - \left(c_{Na^+} + c_{NaHCO_3aq} \right) = 0 \qquad (A.8)$$

719
$$u_{CO_2} - \left(c_{CO_2aq} + c_{H^+} - c_{OH^-} - c_{CO_3^{2-}} \right) = 0 \qquad (A.9)$$

720
$$c_{Ca^{2+}} = u_{Ca} \qquad (A.10)$$

721

40

References

Ahmad N., Wörman A., Bottacin-Busolin A. and Sanchez-Vila X. 2015. Reactive transport modeling of leaking CO_2-saturated brine along a fractured pathway. *Int. J. Greenhouse Gas Cont.* **42**, 672-689. http://dx.doi.org/10.1016/j.ijggc.2015.09.001.

Andreani M., Gouze P., Luquot L. and Jouanna P. 2008. Changes in seal capacity of fractured claystone caprocks induced by dissolved and gaseous CO_2 seepage. *Geophys. Res. Lett.* **35**, L14404. doi:10.1029/2008GL034467.

Aradóttir E.S.P., Sonnenthal E.L., Björnsson G. and Jónsson H. 2012. Multidimensional reactive transport modeling of CO_2 mineral sequestration in basalts at the Hellisheidi geothermal field, Iceland. *Int. J. Greenhouse Gas Cont.* **9**, 24-40.

Bachu S., Gunter W.D. and Perkins E.H. 1994. Aquifer disposal of CO_2: hydrodynamic and mineral trapping. *Energ. Convers. Manage.* **35(4)**, 269-279.

Basirat F., Sharma P., Fagerlund F. and Niemi A. 2015. Experimental and modeling investigation of CO2 flow and transport in a coupled domain of porous media and free flow. *Int. J. Greenhouse Gas Cont.* **42**, 461-470.

Bear J., 1972. *Dynamics of Fluids in Porous Media*. ISBN-13: 978-0-486-65675-5, Elsevier, New York.

Bear J. and Cheng A.H.-D. 2010. *Modeling groundwater flow and contaminant transport.* Vol. **23**, ISBN, 978-1-4020-6681-8, Springer, Dordrecht. doi:10.1007/978-1-4020-6682-5.

Bethke C.M. 2008. *Geochemical and Biogeochemical Reaction Modeling.* Second ed., ISBN-13 978-0-511-37897-3. Cambridge University Press, New York.

Bodin J., Delay F. and de Marsily G. 2003. Solute transport in a single fracture with negligible matrix permeability: 2. Mathematical formalism. *Hydrogeol. J.* **11 (4)**, 434-454. doi:10.1007/s10040-003-0269-1.

Chabonan M., David B. and Boyeau B. 2015. Averaged model for momentum and dispersion in hierarchical porous media. *Phys. Rev.* **E 92(2)**, 023201.

COMSOL. The Platform for Physics-Based Modeling and Simulation. COMSOL Inc. AB, Stockholm, Sweden, http://www.comsol.com/.

Cvetkovic V., Selroos J.O. and Cheng H. 1999. Transport of reactive tracers in rock fractures. *J. Fluid Mech.* **378**, 335-356. doi:10.1017/S0022112098003450.

Delany J.M. and Lundeen S.R., 1990, The LLNL thermochemical database. Lawrence Livermore National Laboratory Report UCRL-21658, 150 p.

Dreybrodt W., Eisenlohr L., Madry B. and Ringer S. 1997. Precipitation kinetics of calcite in the system $CaCO_3$-H_2O-CO_2: The conversion to CO_2 by the slow process $H^+ + HCO_3^- \rightarrow CO_2 + H_2O$ as a rate limiting step. *Geochemica et Cosmochimica Acta*, **61(18)**, 3897-3904.

Dreybrodt W., Lauckner J., Zaihua L., Svensson U. and Buhmann D. 1996. The kinetics of the reaction in the $CO_2 + H_2O \rightarrow H^+ + HCO_3^-$ as one of the rate limiting steps for the dissolution of calcite in the system H_2O-CO_2-$CaCO_3$. *Geochemica et Cosmochimica Acta*, **60(18)**, 3375-3381.

Duan Z. and Sun R. 2003. An improved model calculating CO_2 solubility in pure water and aqueous NaCl solutions from 273 to 533 K and from 0 to 2000 bar. *Chem. Geol.* **193 (3-4)**, 257-271. doi:10.1016/S0009-2541(02)00263-2.

Duan Z., Sun R., Zhu C. and Chou I. 2006. An improved model for the calculation of CO_2 solubility in aqueous solutions containing Na^+, K^+, Ca^{2+}, Mg^{2+}, Cl^-, and SO_4^{2-}. *Mar. Chem.* **98 (2-4)**, 131-139. doi:10.1016/j.marchem.2005.09.001.

Ellis B.R., Bromhal G.S., McIntyre D.L. and Peters C.A. 2011a. Changes in caprock integrity due to vertical migration of CO_2-enriched brine. *Energ. Procedia* **4**, 5327-5334.

Ellis B., Peters C., Fitts J., Bromhal G., McIntyre D., Warzinski R. and Rosenbaum E., 2011b. Deterioration of a fractured carbonate caprock exposed to CO_2-acidified brine flow. *Greenhouse Gas: Sci Technol.* **1**, 248-260.

Fujii T., Nakagawa S., Sato Y., Inomata H. And Hashida T. 2010. Sorption characteristics of CO_2 on rocks and minerals in storing CO_2 processes. Natural Res. **1 (1)**, 1-10.

Gaus I. 2010. Role and impact of CO_2-rock interactions during CO_2 storage in sedimentary rocks. *Int. J. Greenh. Gas Con.* **4 (1)**, 73-89. doi:10.1016/j.ijggc.2009.09.015.

Gelhar L.W., Welty C. and Rehfeldt K.R. 1992. A critical review of data on field-scale dispersion in aquifers. *Water Resour. Res.*, **28(7)**, 1955-1974.

Gherardi F., Xu T. and Pruess K. 2007. Numerical modeling of self-limiting and self-enhancing caprock alteration induced by CO_2 storage in a depleted gas reservoir. *Chem. Geol.* **244 (1-2)**, 103-129. doi:10.1016/j.chemgeo.2007.06.009.

Gislason S.R. and Oelkers E.H. 2014. Carbon storage in Basalt. *Science* **344**, 373. doi: 10.1126/science.1250828.

Grisak G.E. and Pickens J.F. 1980. Solute transport through fractured media 1. The effect of matrix diffusion. *Water Resour. Res.* **16 (4)**, 719-730.

Golfier F., Lasseux D. and Quintard M. 2015. Investigation of the effective permeability of vuggy or fractured porous media from a Darcy-Brinkman approach. *Comput. Geosci.* **19**, 63-78.

Goyeau G., Lhuillier D., Gobin D. and Velarde M.G. 2003. Momentum transport at a fluid-porous interface. *Int. J. Heat Mass Transfer* **46**, 4071-7081.

Gulbransen A.F., Hauge V.L. and Lie K.-A. 2008. A multiscale mixed finite-element method for vuggy and naturally-fractured reservoirs. 21 Nordic Seminar on Computational Mechanics, NSCM-21.

Haugan P.M. and Joos F. 2004. Metrics to assess the mitigation of global warming by carbon capture and storage in the ocean and in geological reservoirs. *Geophys. Res. Lett.* **31**, L18202.

Heller R. and Zoback M. 2014. Adsorption of methane and carbon dioxide on gas shale and pure mineral samples. *Unconventional Oil Gas Resour.* 8, 14-24.

Holloway S. 2005. Underground sequestration of carbon dioxide-a viable greenhouse gas mitigation option. *Energy* **30** **(11-12)**, 2318-2333. doi:10.1016/j.energy.2003.10.023.

Intergovernmental Panel of Climate Change, 2005. IPCC Special Report on Carbon Dioxide Capture and Storage. Cambridge University Press, New York, America.

Jamet D., Chandesris M. and Goyeau B. 2009. On the equivalence of the discontinuous one- and two-domain approaches for the modeling of transport phenomena at a fluid/porous interface. *Transp. Porous Med.* **78**, 403-418.

Johnson J.W., Nitao J.J. and Knauss K.G. 2004. Reactive transport modelling of CO_2 storage in saline aquifers to elucidate fundamental processes, trapping mechanisms, and sequestration partitioning. Geological Society of London Special Publication on Carbon Sequestration Technologies.

Kaufmann G. and Dreybrodt W. 2007. Calcite dissolution kinetics in the system $CaCO_3$-H_2O-CO_2 at high undersaturation. *Geochim. et Cosmochim. Acta* **71 (6)**, 1398-1410. doi:10.1016/j.gca.2006.10.024.

Lai K-H., Chen J-S., Liu C-W. and Yang S-Y. 2014. Effect of permeability-porosity functions on simulated morphological evolution of a chemical dissolution front. *Hydrol. Process*. **28**, 16-24. doi:10.1002/hyp.9492.

Langmuir D. 1997. *Aqueous Environmental Geochemistry*. ISBN 0-02-367412-1, Prentice Hall, New Jersey.

Lasaga A.C. 1984. Chemical kinetics of water-rock interaction. *J. Geophys. Res.* **89 (B6)**, 4009-4025.

Lasaga A.C., Soler J.M., Ganor J., Bruch T.E. and Nagy K.L. 1994. Chemical weathering rate laws and global geochemical cycles. *Geochim. et Cosmochim. Acta* **58 (10)**, 2361-2386.

Laubach SE, Olson JE, Eichhubl P, Fomel S, Marrett RA. 2010. Natural Fractures from the perspective of diagenesis. *Canadian Society of Exploration Geophysicists, CSEG RECORDER*, September 2010.

Lide D.R. ed., 2010. *CRC Handbook of Chemistry and Physics*. 90th Edition (CD-ROM Version 2010), CRC Press/Taylor and Francis, Boca Raton, FL.

Liu C., Zhang R., Zhang H., Yang X. and Wang J. 2013. Characteristics and origin of microfracture in lower cretaceous tight sandstone from Kuqa Foreland Basin, NW China. *AAPG Annual Convention and Exhibition, Pittsburgh, Pennsylvania*, May 19-22.

Mao S. and Duan Z. 2009. The viscosity of aqueous alkali-chloride solutions up to 623K, 1000 bar, and high ionic strength. *Int. J. Thermophys*. **30 (5)**, 1510-1523. doi:10.1007/s10765-009-0646-7.

Marini L. 2007. *Sequestration of carbon dioxide; thermodynamics kinetics and reaction path modeling*. ISBN-13:978-0-444-52950-3. Elsevier, Netherlands and UK.

Middleton R.S., Keating G.N., Stauffer P.H., Jordan A.B., Viswanathan H.S. and Kang Q.J. 2012. The cross-scale science of CO_2 capture and storage: from pore scale to regional scale. *Energ. Environ. Sci*. **5 (6)**, 7328-7345. doi:10.1039/c2ee03227a.

Neretnieks I. 1980. Diffusion in the rock matrix: an important factor in radionuclide retardation? *J. Geophys. Res.* **85 (B8)**, 4379-4397. doi:10.1029/JB085iB08p04379.

Nogues J.P., Fitts J.P., Celia M.A. and Peters C.A. 2013. Permeability evolution due to dissolution and precipitation of carbonates using reactive transport modeling in pore networks. *Water Resour. Res*. **49**, 6006-6021. doi:10.1002/wrcr.20486.

Noiriel C., Madé B., and Gouze P., 2007. Impact of coating development on the hydraulic and transport properties in argillaceous limestone fracture. *Water Resour. Res*. **43**, W09406. doi:10.1029/2006WR005379.

Novak C.F. 1993. Modeling mineral dissolution and precipitation in dual-porosity fracture-matrix system. *J. Cont. Hydrol*. **13**, 91-115.

Novak C.F. 1996. Development of the FMT chemical transport simulator: coupling aqueous density and mineral volume fraction to phase compositions. *J. Cont. Hydrol.* **21 (1-4)**, 297-310. doi:10.1016/0169-7722(95)00055-0.

Peters C.A., Fitts J.P., Wilson E.J., Pollak M.F., Bielicki J.M. and Bhatt V. 2014. Basin-scale leakage risks from geologic carbon sequestration: impact on carbon capture and storage energy market competitiveness. Final Scientific/Technical Report, DOE/FE0000749-41, Princeton University, Princeton, NJ, United States.

Popov P., Efendiev Y. And Qin G. 2009. Multiscale modelling and simulations of flows in naturally fractured karst reservoirs. *Commun. Comput. Phys*. **6(1)**, 162-184.

Pruess K. 2006(a). Numerical modeling of CO_2 sequestration in geologic formations-recent results and open challenges. Earth Sciences Division, Lawrence Berkeley National Laboratory, University of Californai, Berkeley, CA 94720, USA.

Pruess K. 2006(b). On leakage from geologic storage reservoirs of CO_2. LBNL-59732. Lawrence Berkeley National Laboratory.

Pruess K. 2008. Leakage of CO_2 from geologic storage: Role of secondary accumulation at shallow depth. *Int. J. Greenh. Gas Con*. **2**, 37-46.

Saaltink M.W., Ayora C. and Carrera J. 1998. A mathematical formulation for reactive transport that eliminates mineral concentrations. *Water Resour. Res.* **34(7)**, 1649-1656.

Sajjadi B., Abdul Aziz A.R., Baroutian S. and Ibrahim S. 2014. Investigation of convection and diffusion during biodiesel production in packed membrane reactor using 3D simulation. *J. Ind. Eng. Chem.* **20**, 1493-1504.

Santschi C.h. and Rossi M.J. 2006. Uptake of CO_2, SO_2, HNO_3 and HCl on calcite ($CaCO_3$) at 300 K: mechanism and the role of adsorbed water. *J. Phys. Chem.* **A 110 (21)**, 6789-6802. doi:10.1021/jp056312b.

Steefel C.I. and Lichtner P.C. 1998(a). Multicomponent reactive transport in discrete fractures I. Controls on reaction front geometry. *J. Hydro*. **209**, 186-199.

Steefel C.I. and Lichtner P.C. 1998(b). Multicomponent reactive transport in discrete fractures II. Infiltration of hyperalkaline groundwater at Maqarin, Jordan, a natural analogue site. *J. Hydro*. **209**, 200-224.

Stone E.J., Lowe J.A. and Shine K.P. 2009. The impact of carbon capture and storage on climate. *Energ. Environ. Sci.* **2 (1)**, 81-91. doi:10.1039/b807747a.

Svensson U. and Dreybrodt W. 1992. Dissolution kinetics of natural calcite minerals in CO_2-water systems approaching calcite equilibrium. *Chem. Geol.* **100**, 129-145.

Tabrizy V.A., Hamouda A.A., Soubeyrand-Lenoir E. and Denoyel R. 2013. CO_2 adsorption isotherm on modified calcite, quartz, and kaolinite surfaces: surface energy analysis. *Pet. Sci. Tech.* **31 (15)**, 1532-1543.

Tao K., Yao J. and Huang Z. 2013. Analysis of the laminar flow in a transition layer with variable permeability between a free-fluid and a porous medium. *Acta Mech.* **224**, 1943-1955.

The GEOCHEMIST'S WORKBENCH®. An integrated geochemical modeling package. Aqueous Solutions LLC, Champaign, IL 61820 USA.

Wealthall G.P., Steele A., Bloomfield J.P., Moss R.H. and Lerner D.N. 2001. Sediment filled fractures in the Permo-Triassic sandstones of the Cheshire basin: observations and implications for pollutant transport. *J. Contam. Hydrol.* **50**, 41-51.

Wu Y-S., Ye M. and Sudicky E.A. 2010. Fracture-flow-enhanced matrix diffusion in solute transport through fractured porous media. *Transp. Porous Med.* **81**, 21-34.

Xu T., Apps J.A. and Pruess K. 2005. Mineral sequestration of carbon dioxide in a sandstone-shale system. *Chem. Geol.* **217**, 295-318.

Xu S., Wörman A. and Dverstorp B. 2001. Heterogeneous matrix diffusion in crystalline rock--implications for geosphere retardation of migrating radionuclides. *J. Contam. Hydrol.* **47 (2-4)**, 365-378.

Xu T., Sonnenthal E., Spycher N. and Zheng L. 2014. TOUGHREACT V3.0-OMP Reference Manual: A parallel simulation program for non-isothermal multiphase geochemical reactive transport. LBNL-DRAFT, Earth Sciences Division, Lawrance Berkeley National Laboratory, University of California, Berkeley, CA 94720.

723